AGU PUBLICATIONS

JGR

Journal of Geophysical Research: Atmospheres

RESEARCH ARTICLE
10.1002/2016JD025914

Key Points:
- Statistical analysis shows that weakly forced mountain-to-plain precipitation systems in the Beijing area propagate on well-defined paths
- Interaction of the cold pool with environmental wind and sea breeze plays a key role in the organization and intensification of convection
- The mountain-to-plain cases have distinct environmental features from those of the null cases

Correspondence to:
X. Xiao,
xxiao@ium.cn

Citation:
Xiao, X., J. Sun, M. Chen, X. Qie, Y. Wang, and Z. Ying (2017), The characteristics of weakly forced mountain-to-plain precipitation systems based on radar observations and high-resolution reanalysis, *J. Geophys. Res. Atmos.*, *122*, 3193–3213, doi:10.1002/2016JD025914.

Received 12 SEP 2016
Accepted 25 FEB 2017
Accepted article online 2 MAR 2017
Published online 17 MAR 2017

The characteristics of weakly forced mountain-to-plain precipitation systems based on radar observations and high-resolution reanalysis

Xian Xiao[1,2,3], Juanzhen Sun[4], Mingxuan Chen[2], Xiushu Qie[1,3], Yingchun Wang[5], and Zhuming Ying[4]

[1]Key Laboratory of Middle Atmosphere and Global Environment Observation, Institute of Atmospheric Physics, Chinese Academy of Sciences, Beijing, China, [2]Institute of Urban Meteorology, China Meteorological Administration, Beijing, China, [3]University of Chinese Academy of Sciences, Beijing, China, [4]National Center for Atmospheric Research, Boulder, Colorado, USA, [5]Beijing Meteorological Service, China Meteorological Administration, Beijing, China

Abstract The metropolis of Beijing in China is located on a plain adjacent to high mountains to its northwest and the gulf of the Bohai Sea to its southeast. One of the most challenging forecast problems for Beijing is to predict whether thunderstorms initiating over the mountains will propagate to the adjacent plains and intensify. In this study, 18 warm season convective cases between 2008 and 2013 initiating on the mountains and intensifying on the plains under weak synoptic forcing were analyzed to gain an understanding of their characteristics. The statistical analysis was based on mosaic reflectivity data from six operational Doppler radars and reanalysis data produced by the Four-Dimensional Variational Doppler Radar Analysis System (VDRAS). The analysis of the radar reflectivity data shows that convective precipitation strengthened on the plains at certain preferred locations. To investigate the environmental conditions favoring the strengthening of the mountain-to-plain convective systems, statistical diagnoses of the rapid-update (12 min) 3 km reanalyses from VDRAS for the 18 cases were performed by computing the horizontal and temporal means of convective available potential energy, convective inhibition, vertical wind shear, and low-level wind for the plain and mountain regions separately. The results were compared with those from a baseline representing the warm season average and from a set of null cases and found considerable differences in these fields between the three data sets. The mean distributions of VDRAS reanalysis fields were also examined. The results suggest that the convergence between the low-level outflows associated with cold pools and the south-southeasterly environmental flows corresponds well with the preferred locations of convective intensification on the plains.

1. Introduction

The forecasting of convective systems in the warm season and their associated severe weather phenomena, especially in large metropolitan areas with complex underlying terrain, remains a challenging scientific problem. Our study aims to investigate the statistical characteristics and enhancement mechanisms of convective systems that travel from mountains to adjacent plains in the Beijing area of China in the absence of strong synoptic forcing, using radar observations and high-resolution reanalyses obtained from a four-dimensional variational (4DVAR) data assimilation system. In recent decades, numerous studies have sought to gain an understanding of the statistical characteristics (e.g., diurnal variation) of midlatitude warm season convective precipitation. These studies have either used long-term observational data from surface stations, radars, satellites, and lightning maps, or numerical models [*Steiner et al.*, 1995; *Carbone et al.*, 2002; *Davis et al.*, 2003; *Wang et al.*, 2004; *Murphy and Konrad*, 2005; *Carbone and Tuttle*, 2008; *Overeem et al.*, 2009; *Koo and Hong*, 2010; *Surcel et al.*, 2010; *Lin et al.*, 2011]. Most of these studies have shown that the spatial and temporal patterns of diurnal variation in convective precipitation vary with the local topography.

Beijing is a metropolis with complex underlying terrain that is high to the northwest, where the highest peak of the Yanshan mountain range is over 2600 m, and low to the southeast (Figure 1a). Furthermore, sea breezes from the Bohai Sea to the east of Beijing and Tianjin also influence these cities. Such a complex terrain plays an important role in the generation of convective activity in the Beijing area. *Chen et al.* [2012, 2014] examined the climatology of warm season precipitation in Beijing and its vicinity

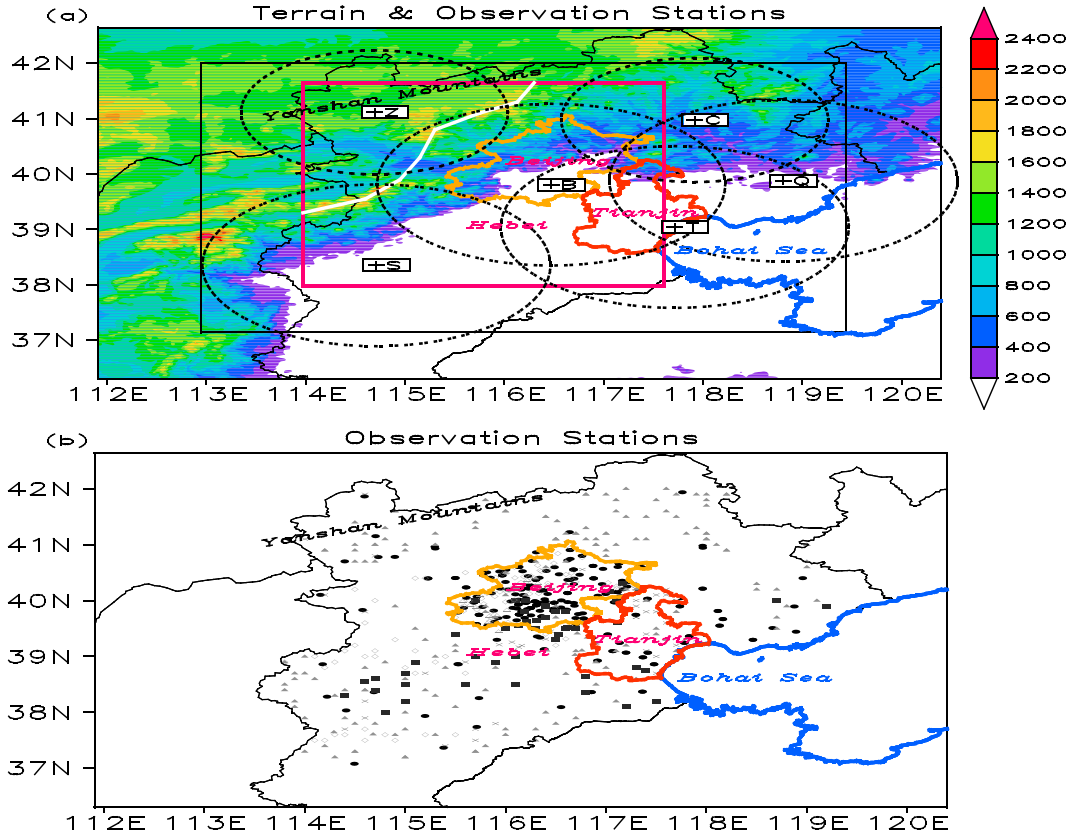

Figure 1. (a) Surface elevation (m) around the study area in contiguous north China. The solid black rectangle is the VDRAS reanalysis domain of 540 km × 540 km, and the red rectangle is the domain used for calculating the mean wind, CAPE, and CIN in Figures 5 and 6. The white line is used for selecting the cases described in section 2. The six radar sites of the operational CINRAD network are indicated (plus symbols) with the letter B standing for BJRS, T for TJRS, S for SJZRS, Z for ZBRC, C for CDRC, and Q for QHDRS. The thick blue line indicates the coastline, the red and orange lines are the boundaries of Tianjin and Beijing, respectively, and the black line indicates the provincial border. (b) Location of Mesonet stations, filled circle, cross, filled square, diamond, and filled rectangle stand for surface automated weather stations installed in 2009, 2010, 2011, 2012 and 2013, respectively.

using multiyear radar reflectivity data. They found that warm season convective activity had a clear correlation with terrain orientation. Further analysis by *Chen et al.* [2014] revealed two dominant propagation paths of the convective systems: northwest to southeast and southwest to northeast, and the two showed marked differences in precipitation characteristics and occurred under different large-scale regimes. Further climatology analysis of summer heavy rainfall events over Beijing metropolitan by *Yang et al.* [2014a, 2014b] showed that the urbanization might have played a role in shifting the location of heavy rainfall.

Although all convective systems pose challenges to forecasters, one of the most difficult forecast problems in the Beijing area is to predict whether the thunderstorms that initiate over nearby mountains will propagate to the plains and intensify [*Wilson et al.*, 2010]. *Huang* [2012] found that more than 40% of summertime convective systems that affected the Beijing area formed in the northwestern mountain area. These systems then intensified or dissipated when propagating eastward or southeastward. According to their study, nearly 30% of these systems intensified into severe storms with heavy rain as they propagated to the plains where Beijing is located, while others remained in the mountains or dissipated as they entered the plains. Some of the intensified systems on the plains became organized into linear systems and had a longer lifetime. Under strong synoptic forcing, the radar data show organized convection over the mountains, but under weak synoptic forcing the radar indicates scattered convective clusters. These clusters can either organize/intensify as they propagate to the plains, or simply dissipate before they reach the plains, posing a forecast problem. In the former case, heavy rains often influence urban Beijing, bringing

Table 1. Large-Scale Environment for Selected MTP Cases

Date	500 hPa	850 hPa
23 Jun 2008	Mongolia vortex	Weak trough
27 Jun 2008	Dongbei vortex	Shortwave trough
4 Sep 2008	Weak trough	Weak ridge
16 Sep 2008	Weak ridge	Weak ridge, jet scream
5 Jul 2009	Mongolia vortex	Weak vortex
19 Jul 2009	Shortwave trough	West of high pressure
22 Jul 2009	Left side of trough	Right side of ridge
23 Jul 2009	Shortwave trough	Shear line
1 Aug 2009	Weak trough	Shear line
9 Aug 2009	Right side of trough	Shear line
11 Jun 2011	Shortwave trough	Shear line
23 Jun 2011	Shortwave trough	Shear line
7 Jul 2011	Low	Low
9 Jun 2012	Mongolia vortex	Right side of trough
28 Jun 2013	Shortwave trough	West of high pressure
30 Jul 2013	Right side of weak ridge	Weak ridge
31 Jul 2013	Mongolia vortex	Shortwave trough
4 Aug 2013	Right side of weak ridge	Left side of weak ridge

flooding, strong wind, hail, and lightning [*Liu et al*., 2011]. Because of the urban expansion and increased population, it is more challenging for big cities to avoid meteorology disasters such as flood, lightning, and urban waterlogging [*Liu et al*., 2013; *Hu*, 2015]. Improving the forecasting problem will doubtless result in great social and economical benefit.

By examining mean observations from a single sounding, *Wilson et al*. [2010] and *Chen et al*. [2014] found that a persistent warm southeasterly wind over the plains was key for the enhancement of convection near the foothills. However, their studies did not identify the characteristics and dynamical processes that contributed to enhancement on the plains. Recent studies have shown that not only synoptic conditions but also local thermodynamics play important roles in the distribution and evolution of storms in the Beijing area [*He and Zhang*, 2010; *Miao et al*., 2011]. While these studies are important, they only provide a qualitative picture of storm intensification on the plains and lack detailed information that could help improve our understanding of the important environmental conditions and mesoscale features necessary for the mountain-to-plain (MTP) propagation of convection. To address this shortcoming, in this study we conduct a statistical analysis of 18 MTP convective cases that initiated over the mountains under weak synoptic forcing. Specifically, we attempt to answer these two questions: What are the statistical characteristics of MTP storm propagation in the absence of strong synoptic forcing? What are the statistical characteristics of the environment and of the 3-D dynamical and thermal fields that play dominant roles in the process of MTP storm intensification?

To answer these questions, we use radar data from China's operational CINRADs (China Next Generation Weather Radar) in the study region and reanalysis data from the Variational Doppler Radar Analysis System (VDRAS), which was developed by the National Center for Atmospheric Research [*Sun and Crook*, 1997, 2001; *Sun et al*., 2010]. This system produces high-resolution analyses updated every 5–15 min by assimilating radar and surface observations using the 4DVAR data assimilation technique and a cloud model. Through the 4DVAR data assimilation of radial velocity and reflectivity from multiple radars, VDRAS retrieves the meteorological fields that are not observed by Doppler radar (e.g., 3-D wind, temperature, shear, divergence, and CAPE (convective available potential energy)/CIN (convective inhibition)). Since 2008, the Beijing Meteorological Service (BMS) has been running VDRAS operationally in its forecast office to assist convective weather nowcasting, with modifications [*Sun et al*., 2010] to accommodate the local observation networks. Besides its operational applications since 2001 [*Sun and Crook*, 2001], VDRAS has also been used for case studies of convective storms [i.e., *Sun*, 2005; *Sun and Zhang*, 2008; *Tai et al*., 2011; *Friedrich et al*., 2015; *Gochis et al*., 2015; *M. Chen et al*., 2016]. In the present study, we use the rapid-update VDRAS analyses to derive statistical properties of the MTP convective systems in order to gain an understanding of the mesoscale dynamical and thermal features of these systems. The ultimate objective is to improve forecasts by establishing a conceptual model for the MTP convective systems that frequently occur in Beijing.

This paper is divided into seven sections. In section 2, we describe the criteria for selecting the MTP cases with weak synoptic forcing that are used in our statistical analyses. The statistical characteristics of the convective precipitation in the selected cases are described in section 3. The configuration and validation of VDRAS are presented in section 4, and section 5 describes the mean environmental conditions on the mountains and on the plains. Section 6 examines the mesoscale dynamical and thermal characteristics of the MTP storms obtained from VDRAS analyses. Finally, a summary and conclusions are provided in section 7.

Table 2. Large-Scale Environment for Selected Null Cases

Date	500 hPa	850 hPa
18 Jun 2013	West of high pressure	Shear line
23 Jun 2013	West jet scream	Low
27 Jun 2013	Left side of trough	Low
13 Jul 2013	West jet scream	Weak vortex
20 Jul 2013	Shortwave trough	Right side of ridge
8 Aug 2013	Dongbei vortex	Dongbei vortex
13 Aug 2009	Mongolia vortex	LOW
14 Aug 2009	Donbei vortex	West jet scream

2. Criteria for Selecting MTP Convective Cases

In this paper, the warm season is defined as the period from 15 June to 15 September, during which most convective storms occur in the study region (see Figure 1a). Eighteen convective episodes between 2008 and 2013 were selected to include days in which storms propagate from the mountains to the plains (hereafter called MTP case days). Our emphasis is on warm season storms initiated on the mountains without strong synoptic forcing. Furthermore, we focus on storm systems that are intensified into convective lines when they propagate to the plains. The rules for selecting the MTP case days are summarized below. Note that the reflectivity referred to below is a 2-D column maximum field over all elevation scans with a

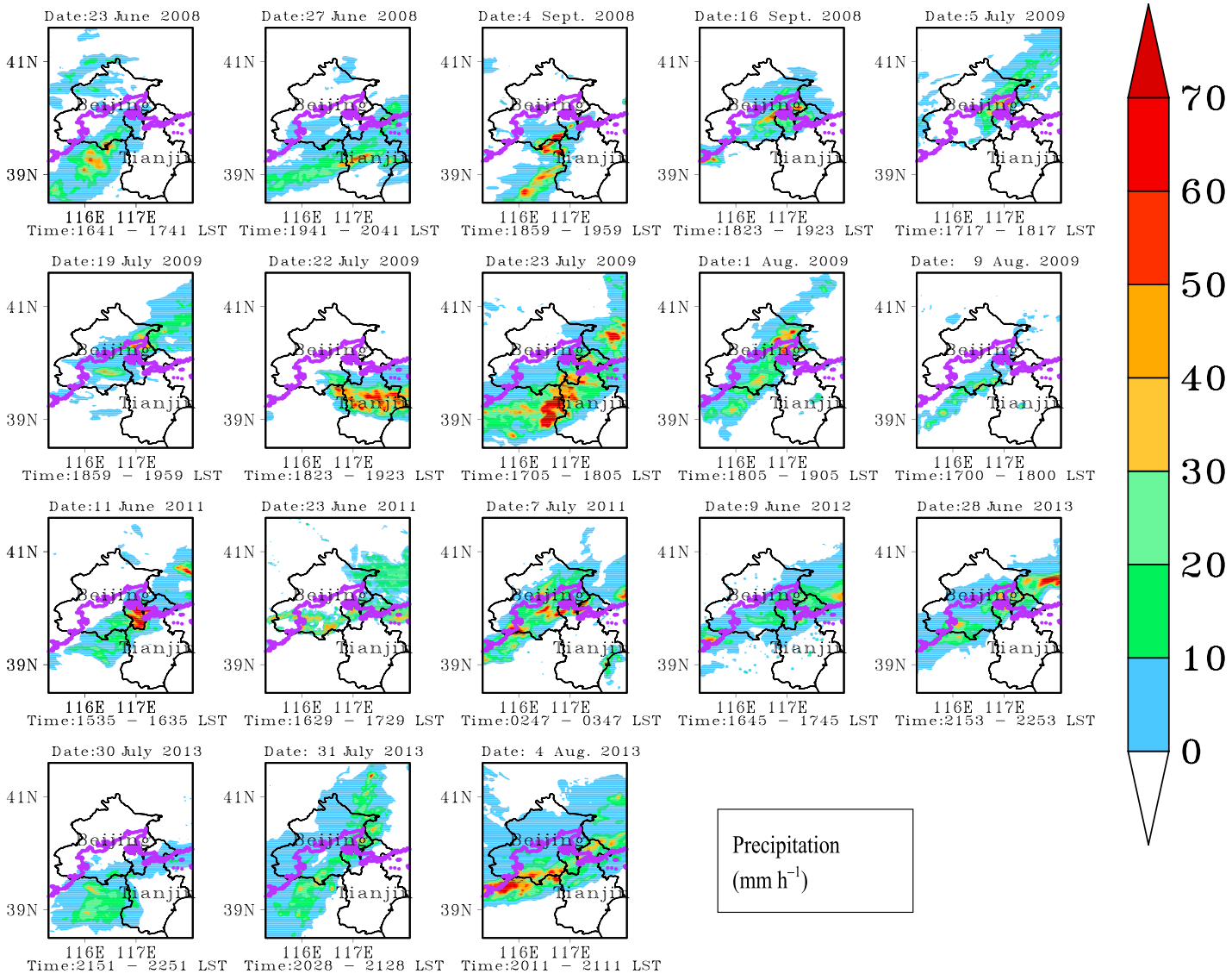

Figure 2. Overview of the 18 MTP cases as represented by hourly precipitation amount (color shading; mm h^{-1}) from surface observations. The black line indicates the city/provincial borders. The thick purple line is the 200 m topographic contour.

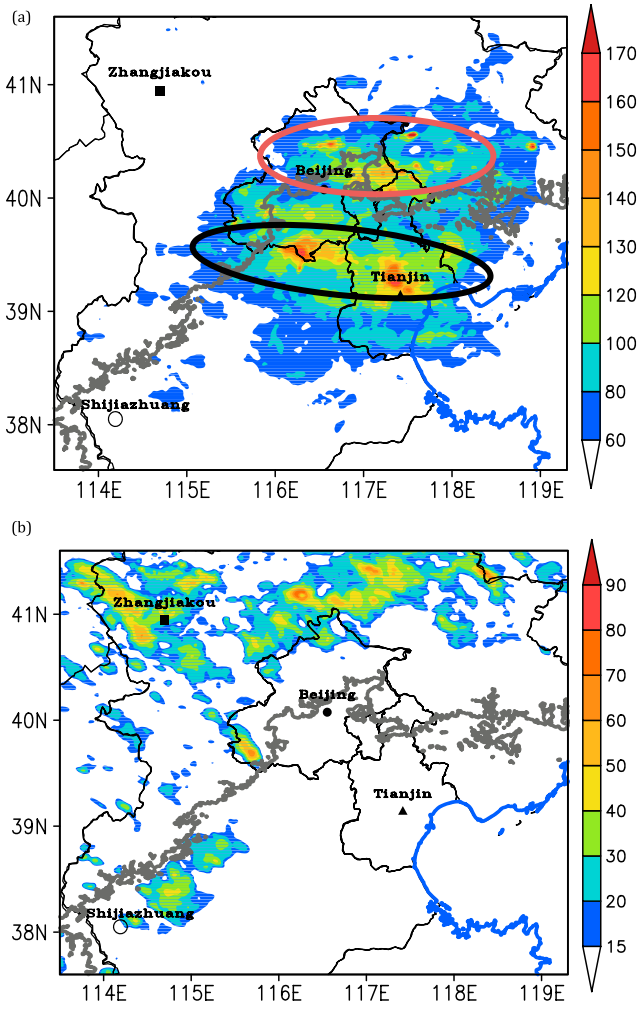

Figure 3. Distribution of occurrence frequency of 40 dBZ reflectivity (number of reflectivities greater than 40 dBZ out of all MTP radar composites) for the (a) 18 MTP convective storms and (b) 8 NULL. The thick gray line is the 200 m topographic contour. The black and red ellipses denote the two high-storm-frequency tracks.

uniform horizontal resolution of 1 km. A quality control procedure for radar reflectivity was performed before the 2-D field was generated.

1. The strong synoptic forcing often exhibited by a north-to-south oriented deep trough over north China is not present.
2. The maximum reflectivity in the VDRAS analysis domain must exceed 35 dBZ (to define a storm event [*Wilson et al.*, 2010]) when a convective system passes the highest mountain ridges (thick white line in Figure 1) before it reaches the foothills. However, reflectivity exceeding 35 dBZ must cover fewer than 90 grid points (90 km^2) and reflectivity exceeding 45 dBZ (to define a heavy storm event [*Mather et al.*, 1976]) must cover fewer than 30 grid points (30 km^2) before the convective system reaches the foothills. This latter criterion is to exclude systems that are already organized over the mountains under strong synoptic forcing.
3. After a convective system reaches the plains, the intensified system must have a 35 dBZ area exceeding 150 grid points (150 km^2) and maximum echoes exceeding 55 dBZ. In addition, the area of radar reflectivity above 35 dBZ must show a clear linear pattern with a length:width ratio above 3:1 at some time over the plains. The reason for selecting linear systems is that they are often frequently associated with high-impact weather in the Beijing area according to statistics from the BMS [*Huang*, 2012].

The 18 cases between 2008 and 2013 satisfying these requirements are listed in Table 1 together with the weather patterns at 500 and 850 hPa, which indicate that the large-scale environment is primarily weakly structured without strong synoptic forcing at 500 and 850 hPa. The Dongbei and Mongolia vortices referred in the Table are vortices that often appear in northeastern China and Mongolia [*He et al.*, 2007; *Ji et al.*, 2008].

Apart from the 18 MTP cases, we also selected 8 convective days (see Table 2) from the summer of 2013 in which the mountain-initiated storms did not reach the plains and named them as null cases (or NULL hereafter). These null cases must meet rules 1 and 2, but do not meet rule 3. Moreover, the cases must originate at the northwest of the mountain area similar to MTP. This restriction allows us to compare the storms with similar initiation mechanisms between MTP and NULL.

The peak 60 min precipitation amount is shown in Figure 2 for the 18 MTP cases based on BMS's Quantitative Precipitation Analysis that combines rainfall from ~150 automated weather stations located in Beijing and Tianjin (Figure 1b) and estimated rainfall from radar. The overview of the 18 cases clearly shows that areas of heavy rain are located northeast or southwest of Beijing. The precipitation peaks of all these convective

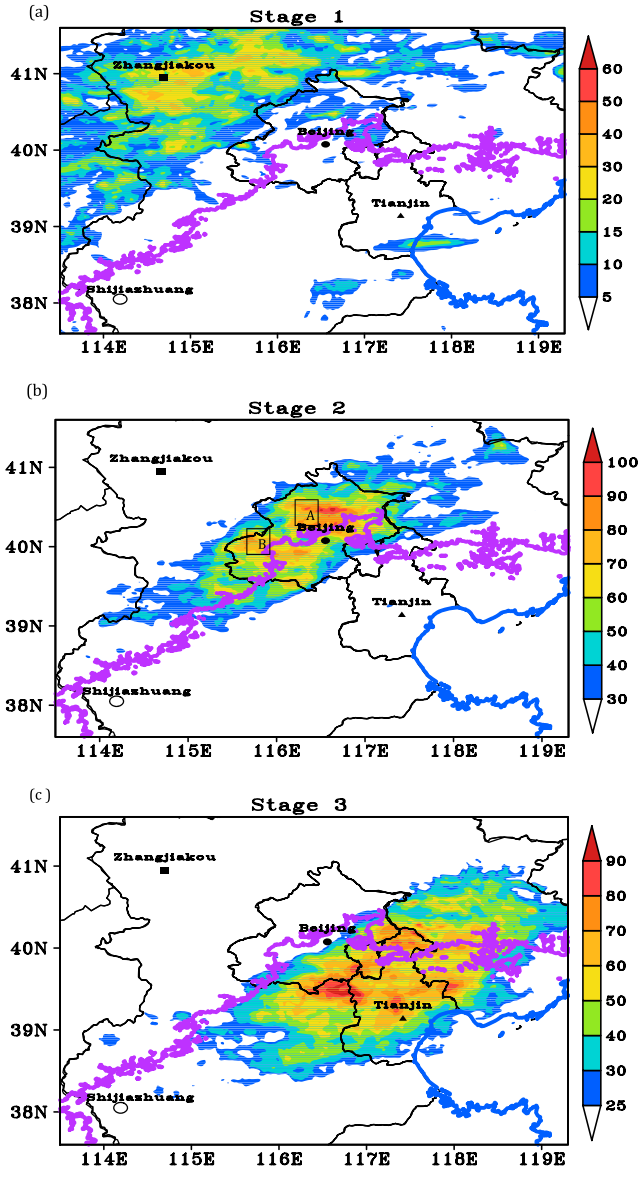

Figure 4. Distribution of 40 dBZ frequency of occurrence (number of reflectivities greater than 40 dBZ out of all MTP radar composites) for the three stages with stage 1 covering the −4, −3, and −2 MTP hours, stage 2 the −1, 0, and +1 MTP hours, and stage 3 the +2, +3, and +4 MTP hours in different color bar. The black contours indicate the city/provincial borders. The thick purple solid contour indicates the elevation of 200 m.

events occur after 1600 local solar time (LST). Fifteen of them have strongest precipitation in the afternoon between 1600 and 2200 LST, while the other three have peaks around midnight.

3. Statistical Characteristics of the Selected MTP Cases

3.1. Spatial Distribution of the Occurrence Frequency of Convective Precipitation

We first examine the spatial distribution of convective precipitation on the MTP case days by computing the occurrence frequency of convective precipitation. Following previous studies [e.g., *Rickenbach and Rutledge*, 1998; *Parker and Knievel*, 2005; *Chen et al*., 2012], the value of 40 dBZ is used as the reflectivity threshold for convective precipitation. The 1 km resolution composite reflectivity of column maximum obtained from four S band radars at Beijing (BJRS), Tianjin (TJRS), Shijiazhuang (SJZRS), and Qinhuangdao (QHDRS), and two C band radars at Chengde (CDRC) and Zhangbei (ZBRC) was used for the statistical computation. The locations of these radars are shown in Figure 1. The temporal resolution of 6 min for the composite reflectivity in the 18 MTP cases gave a total sample size of 1211. The frequency of occurrence of convective precipitation is defined by the number of occurrences of reflectivity greater than 40 dBZ on each grid point. The results are shown in Figure 3 over the VDRAS analysis domain (540 km × 540 km) for both MTP and NULL.

We observe the following features from Figure 3a. First, the frequency is substantially lower over the mountains to the west of Beijing than over the plains. The higher frequency of convective precipitation begins over the foothills and extends to the plains in the east. Second, the higher frequency of storms appears in three areas: southeast of Beijing near its border, central Tianjin, and northeast of Beijing near the foothills of the mountain

Table 3. Average Storm Area (km^2)

	MTP		NULL	
	> = 35 dBZ	> = 45 dBZ	> = 35 dBZ	> = 45 dBZ
Stage 1	118.4	38.4	256.6	34.3
Stage 2	2712.2	533.5	426.0	160.3
Stage 3	4618.2	902.2	381	73.1

Table 4. Average Max Reflectivity (dBZ)

	MTP	NULL
Stage 1	34.6	38.4
Stage 2	55	56.2
Stage 3	57	33

ranges to its northeast. The frequency pattern in Figure 3a suggests that after the convective systems pass over the western mountain ridges, the convective storm echoes occur along two main paths: east-southeastward and eastward (ellipses in Figure 3). Moreover, on the east-southeastward path there are two centers, one southeast of Beijing and one in the Tianjin urban area. Figure 3a also shows that the precipitation track bypasses the central urban area of Beijing where there is an obvious low frequency, which could be the result of urban thermal and roughness effects [*Dou et al*., 2014; *Yang et al*., 2014b]. In contrast to the frequency distribution of MTP, NULL in Figure 3b shows higher storm frequency over the mountains and foothills but no distinct storm activities on the plains, which is similar to that of stage 1 in MTP (Figure 4a) discussed below.

3.2. Temporal Evolution of MTP Storms

To clearly show the evolution of the MTP storms, we set the zero hour as the hour when the main body of a MTP system crosses the line connecting the mountain ridges (thick white line in Figure 1) and starts its downslope propagation. Hence, negative values represent the hours when the systems are over the mountains and positive values the hours when they are over the foothills and plains. The evolution of the MTP systems from −4 h to +4 h covers the main period of their lifetimes. Hereafter, we use "MTP hours" for timings, referenced to the zero MTP hour. We then divide the evolution of the MTP systems into three stages. Stage 1 is from −4 to −2 MTP hours when the storms initiate over the mountains, stage 2 from −1 to +1 MTP hours when the storms propagate from the mountains to the plains, and stage 3 from +2 to +4 MTP hours when the storms evolve over the plains. The frequency of occurrence of convective precipitation is calculated separately for each of the three stages and is shown in Figure 4.

In stage 1 (Figure 4a), the highest frequency is located near Zhangjiakou over the northwest Yanshan Mountains, indicating the initiation region of the majority of the MTP systems. A comparison with the topographical map (see Figure 1) shows that the high frequency in the initiation stage is located near the ridges of the Yanshan Mountains although a scattered pattern is present over the entire northwest mountain region. We believe that thermal forcing associated with afternoon solar heating on the ridges is responsible for the convective initiation [*Carbone et al*., 2002; *Lin et al*., 2011; *Chen et al*., 2012].

In stage 2 (Figure 4b), the region of frequent convective occurrence is over the foothills and has a northeast-to-southwest orientation, similar to that of the elevation contours. The frequency is significantly higher than in stage 1, indicating the growth of the MTP systems as they approach the foothills. Two high-frequency bands are evident north (A) and southwest (B) of metropolitan Beijing near the foothills. These two bands correspond to the eastward and the east-southeastward paths shown in Figure 3. In stage 3, the two high-frequency bands propagate east/east-southeastward and the area with frequency greater than 30 expands to cover Tianjin, part of Beijing, and part of Hebei. The locations of the high-frequency centers are close to those in Figure 3. A comparison of stage 3 with stage 2 shows a significant increase in frequency near the intersection of Beijing, Tianjin, and Hebei and in metropolitan Tianjin along the east-southeastward path.

To further understand the characteristics of the MTP storms, we used Titan [*Dixon and Wiener*, 1993] to compute the average areas (Table 3) above 35 dBZ and 45 dBZ and the average values (Table 4) of maximum reflectivity at different stages for both the MTP cases and the null cases. From mountains to plains, the area of convection from the MTP cases grows significantly from stage 1 to 2 and continues to grow from stage 2 to 3. Similarly, the maximum reflectivity increases significantly between stage 1 and 2, suggesting that the convection at stage 2 has strengthened and organized. In contrast, the average storm area from the null cases grows only moderately from stage 1 to 2 and

Table 5. Average CAPE (J kg^{-1}) From Real Soundings at 14 LST, NCEP, and VDRAS, and Errors of NCEP and VDRAS CAPE With Respect to the Real Sounding

	Real Soundings	NCEP Soundings	VDRAS Soundings
Average	1800	1628	1726
Average error		172	74
Maximum error		3276	1383
Minimum error		26	7

Table 6. As in Table 5 but for CIN

	Real Soundings	NCEP Soundings	VDRAS Soundings
Average	61	45	35
Average error		16	26
Maximum error		147	146
Minimum error		5	5

shrinks from stage 2 to 3. The maximum reflectivity increases to 56.2 dBZ from stage 1 to 2 and then reduces to 33 dBZ.

While the frequency distribution of the convective precipitation shows clear statistical characteristics, a challenging question is what causes these statistical patterns. To answer this question, we ran VDRAS for the 18 cases to obtain detailed wind and temperature analyses. Before the results are analyzed in section 5 to investigate the dynamical and thermodynamical characteristics of the MTP convective systems, we first describe the VDRAS configuration for the current study and validate the analysis results in section 4.

4. VDRAS Description and Validation

4.1. VDRAS Description and Configuration

VDRAS is a local-scale analysis system based on the 4DVAR data assimilation technique, using radar and surface observations as its main data source and a mesoscale model analysis/forecast as background and boundary conditions. By using a short assimilation window and a cloud model, VDRAS is capable of producing accurate convective-scale analyses [*Sun and Crook*, 1997, 1998; *Crook and Sun*, 2002]. In this study, a 12 min window is used that covers at least two radar scans from each of the six radars assimilated (see Figure 1 for the names and locations of the six radars). These radars are run operationally using the same scan mode, producing reflectivities and radial velocities at nine elevation angles with a volume scan rate of 6 min. The analysis domain covers 540 × 540 km centered on 39.5836°N, 116.1802°E, with 3 km resolution. For this study the vertical resolution of the VDRAS analysis is 0.5 km with 30 layers, with the lowest layer centered at 250 m. The temperature, relative humidity, pressure, and wind from 5 min surface Mesonet data within the VDRAS domain are also assimilated through an objective analysis that is used as a mesoscale background for the 4DVar radar data assimilation. A new method to assimilate the surface data simultaneously with the radar data in the 4DVar cost function has recently been developed by *X. Chen et al.* [2016], but the new scheme has not been adopted in BMS's operational VDRAS. In 2008, there were only 140 of these surface Mesonets. The number increased from 2009 to 2013, with year-by-year numbers of 300, 510, 650, 1013, and 1300 (see Figure 1b). Note that radar observations are not available at all grid points because of the limited horizontal observation range of radar; i.e., the CINRADs are not capable of detecting precipitation at radar ranges exceeding 225 km and clear air echoes beyond ~100 km. In VDRAS, the WRF (Weather Research and Forecasting) forecast is merged with surface data and radar velocity azimuth display profiles to create a mesoscale background. The mesoscale background not only provides the boundary conditions but also a first guess that can fill the gaps in the radar network, resulting in a continuous analysis. A more detailed description of VDRAS can be found in previous studies [*Sun and Crook*, 1997; *Sun and Zhang*, 2008].

To better understand the characteristics of the MTP convective systems, we ran VDRAS not only for the 18 selected MTP cases but also for the null cases. In addition, VDRAS was continuously run every day for the summer of 2013 (15 June to 15 September) using the same configuration as the selected cases. The whole summer run is used to obtain a warm season average (WSA hereafter) as a benchmark to reveal the environmental differences between the MTP days and the warm season.

Table 7. As in Table 5 but for 0–3 km Shear ($m\,s^{-1}$)

	Real Shear	NCEP Shear	VDRAS Shear
Average	10.41	7.29	10.73
Average error		3.12	−0.32
Maximum error		10.19	9.09
Minimum error		0.37	0.1

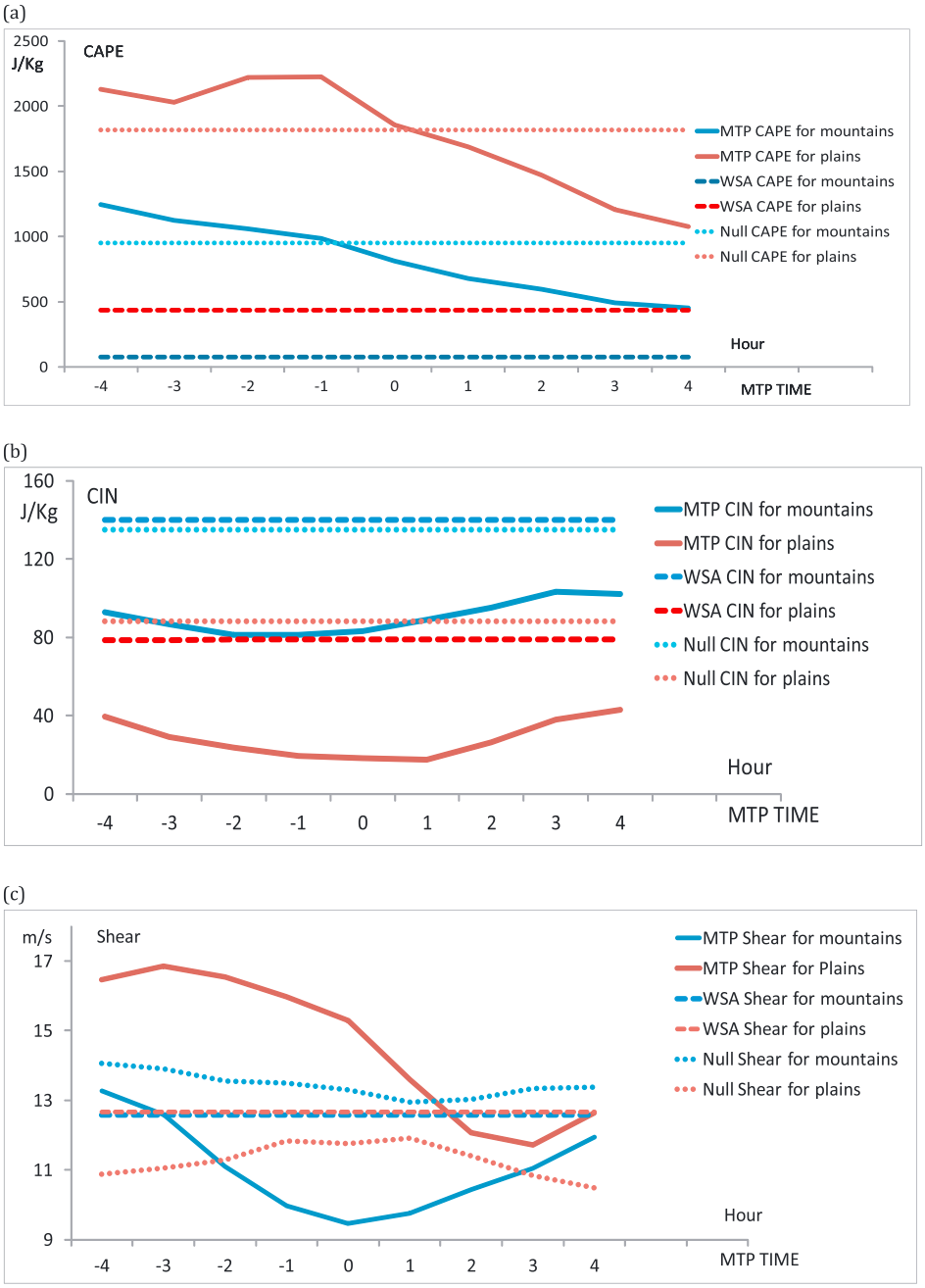

Figure 5. Average (a) CAPE, (b) CIN, and (c) 0–6 km shear with respect to MTP time on the mountains (blue solid lines) and on the plains (red solid lines) for the MTP cases. The dashed lines show the baselines (blue for the mountains and red for the plains) calculated as the warm season average for the summer 2013 season. The dotted lines are the same as the dashed lines but for the NULL cases.

4.2. Validation of VDRAS Reanalysis

The accuracy of the VDRAS wind and temperature analyses has been evaluated in several previous studies against dual-Doppler synthesis [*Crook and Sun*, 2002], profiler, surface data [*Sun et al.*, 2010; *M. Chen et al.*, 2016], radiosonde [*Tai et al.*, 2011], and aircraft data [*Sun and Crook*, 1998]. However, none of these studies verified the derived quantities of CAPE, CIN, and vertical wind shear. Therefore, in the current study we evaluated the accuracy of these diagnostic variables from VDRAS before they are used in our statistical analysis in section 5.

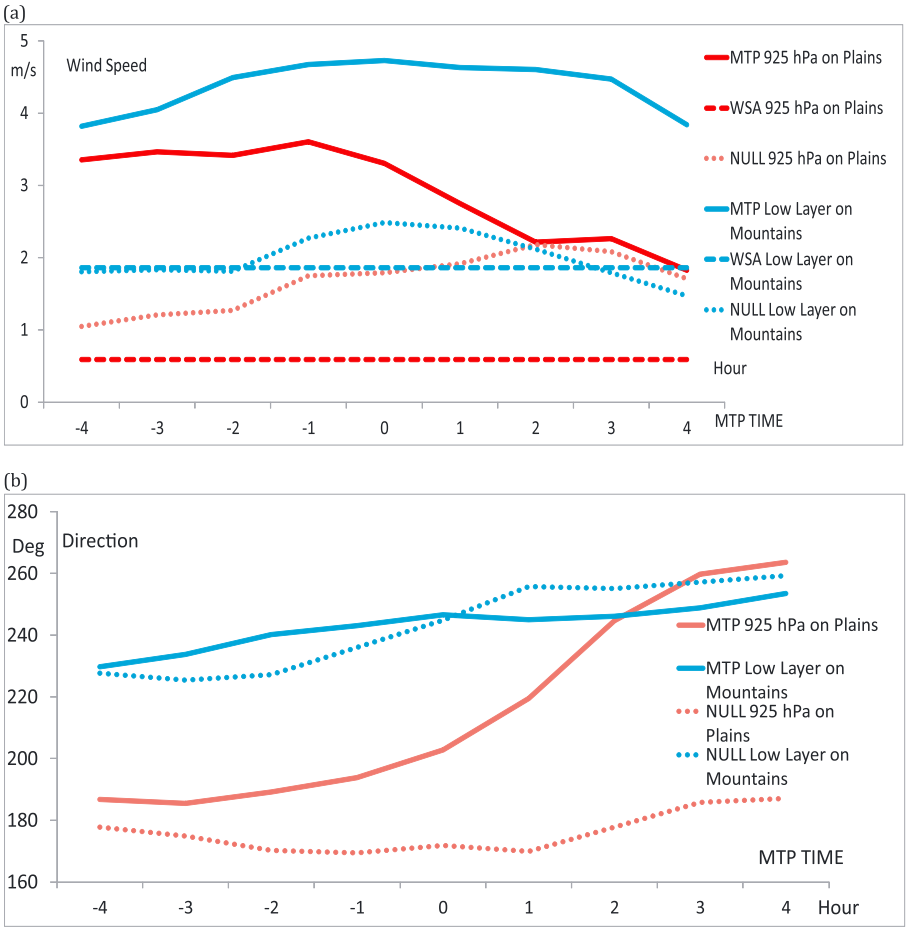

Figure 6. As for Figure 5 but for (a) wind speed and (b) wind direction at the 925 hPa level on the plains and as similar height above the mountains surface (low layer).

An extra sounding is launched at 14 LST (06 UTC) during warm seasons at the Beijing station nearly colocated with BJRS (see Figure 1). This sounding is a good choice for our verification because it is in the early afternoon before the convective initiation. The validation was carried out for the 18 MTP cases. We first evaluate the accuracy of CAPE and CIN. For comparison purposes, these two variables were also computed using National Centers for Environmental Prediction (NCEP) reanalysis data and are listed in Tables 5 and 6, respectively, along with those calculated from the radiosonde and VDRAS reanalysis. The soundings of the NCEP and VDRAS analyses were extracted from grid points nearest to the radiosonde station.

The comparison in Table 5 shows that the mean deviation of CAPE between the NCEP sounding and the radiosonde is 172 J kg^{-1}. The maximum error is as high as 3276 J kg^{-1} while the minimum error is 26 J kg^{-1}. In contrast, the mean deviation of CAPE between the VDRAS sounding and the radiosonde is approximately 74 J kg^{-1}, much smaller than for the NCEP reanalysis, and both the maximum error (1383 J kg^{-1}) and the minimum error (7 J kg^{-1}) are significantly smaller than those of NCEP.

The mean difference in CIN (Table 6) between the radiosonde and NCEP sounding is 16 J kg^{-1} with the largest error approximately 147 J kg^{-1} and the minimum error 5 J kg^{-1}. The mean difference in CIN between the radiosonde and VDRAS sounding is 26 J kg^{-1} with the maximum 146 J kg^{-1} and the minimum 5 J kg^{-1}, slightly worse than NCEP.

Shear is also an important index for severe weather, corresponding to the mesoscale kinetic energy exchange from the low to middle atmosphere. The wind profiler has the advantage over soundings in that it provides a true vertical shear profile while the sounding profile is often skewed because of wind drift. Therefore, we use the wind profiler data to represent the real vertical wind structure (the location of the wind profiler is only

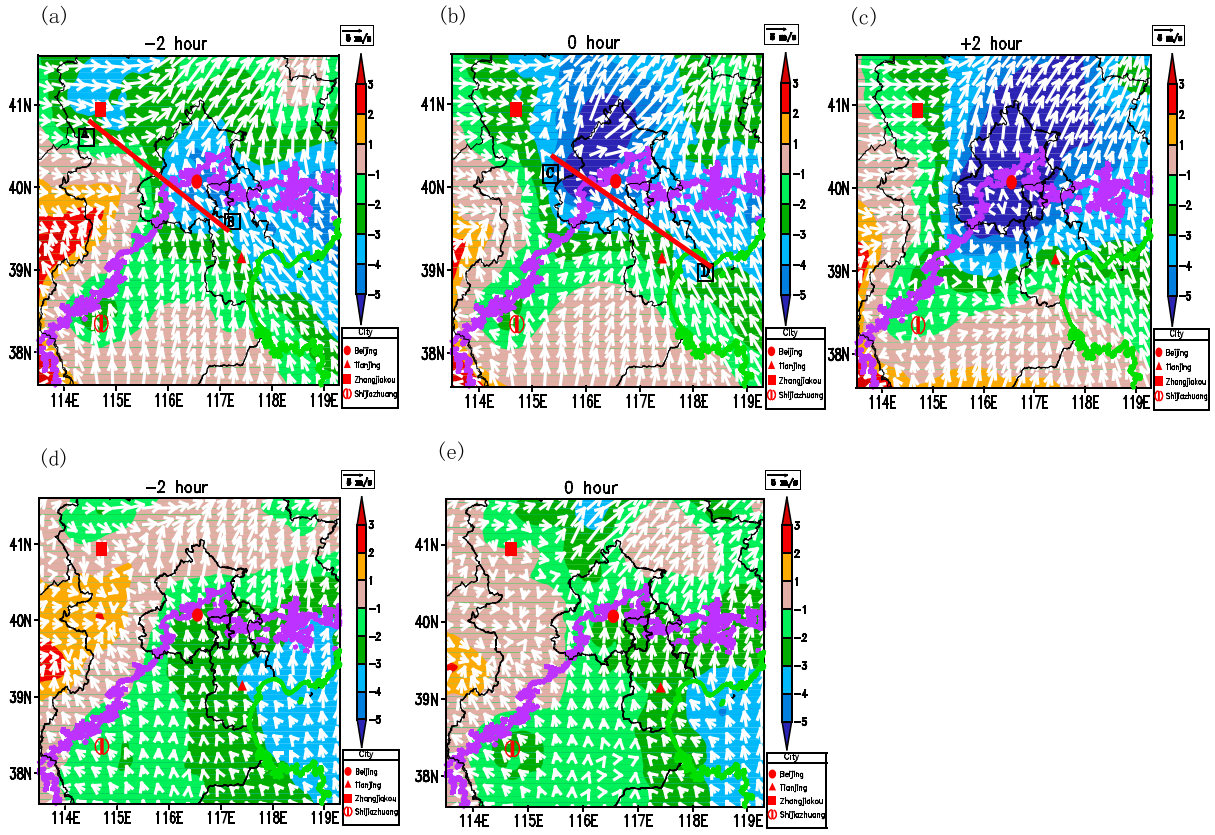

Figure 7. Average perturbation temperature (color shading; °C) shown in the reanalysis domain, overlain with mean wind (vectors) for the MTP hours (a) −2, (b) 0, and (c) +2, while (d) −2 and (e) 0 h of the null cases 250 m above the ground. The thick purple line is the 200 m topographic contour. The green line is the coastline of the Bohai Sea, and the black lines indicate city/provincial borders in north China. The thick red lines indicate the cross sections A–B in Figure 13 and C–D in Figure 14.

200 m away from the BJRS). The computed shear between 3 km and the surface from the wind profiler, NCEP reanalysis, and VDRAS reanalysis are compared in Table 7.

The results in Table 7 show that the mean error between the profiler observations and the NCEP reanalysis is 3.12 m s^{-1}, much larger than that of VDRAS (−0.32 m s^{-1}). Furthermore, both the maximum and minimum errors in VDRAS are smaller than those from the NCEP reanalysis.

In summary, the above verification and comparison demonstrate that the reanalysis of VDRAS has improved accuracy both in the dynamic and thermal fields over the coarser-resolution NCEP reanalysis, which provides a good basis for our diagnostics in the next section. In addition, the frequent VDRAS analyses that are updated every 12 min are capable of depicting the evolution of atmospheric dynamics. Nevertheless, it should be noted that the VDRAS analyses on the mountains inevitably contain larger uncertainties than those on the plains due to not only the difficulty to fully resolve the terrain by the model but also the lack of observations.

5. Thermal and Dynamic Characteristics of the Convective Environment

Using a single sounding in the plains around Beijing, *Wilson et al.* [2010] speculated that the environmental wind and thermal conditions over the plains play an important role in the propagation of storms from the mountains to the plains. However, they were unable to compare the thermal and dynamic conditions between the plains and the mountains, and they could not assess the evolution of storms with time, since the single sounding only represents a single point and time. In the current study using the VDRAS reanalysis, we can separately calculate the average environmental wind and thermal conditions for the mountain and plain regions. In addition, we can compare the MTP case days with the WSA and NULL. The 200 m contour

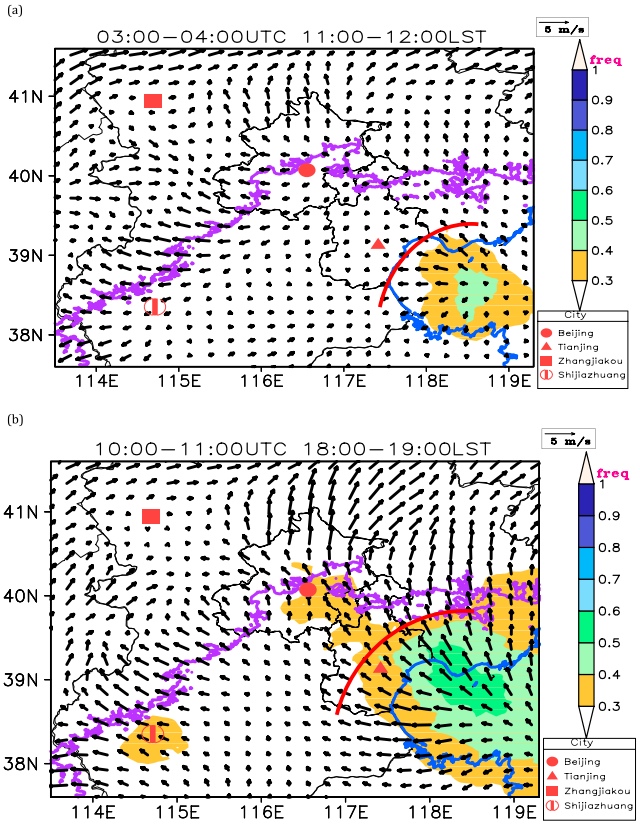

Figure 8. As in Figure 7 but for the spatial distribution of the occurrence frequency (freq) of a cold pool with perturbation temperature < -3°C, overlain by the WSA wind vectors for (a) 3–4 UTC and (b) 10–11 UTC. The thick red line denotes the sea breeze front, and the thick blue line is the coastline of the Bohai Sea.

is used to separate the areas defined as mountains and plains. As in section 3, we set the zero hour as the hour when the main body of a MTP system has passed the line of the mountain ridges (thick white line in Figure 1). For both the mountain and plain regions, we used the VDRAS reanalysis to calculate the spatial means of CAPE, CIN, shear, and low-level wind over the 18 MTP cases at the top of each MTP hour. The 925 hPa level was taken for the low-level wind calculation on the plains. The mean height of the 925 hPa level on the plains was then used for the low-level wind calculation on the mountains to ensure that a similar boundary layer height was represented. Similarly, CAPE, CIN, shear, and the low-level wind were also computed for the WSA and NULL to compare with the MTP.

Figures 5a and 5b show the evolutions of the mean CAPE and CIN of the MTP, the WSA, and the NULL for the mountain and plain regions, respectively. The MTP on both the mountains and the plains have much higher CAPE than their respective WSAs, and the difference over the plains is much larger than over the mountains (Figure 5a). The CAPE also shows differences in its temporal evolution over the mountains and plains. The CAPE over the mountains is at its maximum of ~1300 J kg^{-1} at the beginning of the MTP process and decreases gradually thereafter. The gradual decrease is an indication of low-level cooling by convective storms. The CAPE over the plains increases in the first 2 MTP hours, reaching a maximum of nearly 2300 J kg^{-1} between -2 and 0 MTP hours when storms propagate from the mountains to the plains, and decreases thereafter. The strength of the CAPE over the plains is 1.7 times than that over the mountains and noticeably increases during the first few MTP hours. Compared with the MTP, the NULL has lower CAPE in the early MTP hours on the plains (i.e., ~1800 versus ~2300 J kg^{-1} at -1 MTP hours) but only slightly lower CAPE on the mountains. Nevertheless, unlike the MTP, the CAPEs for NULL maintain their levels for the entire period, consistent with the fact that no convective initiation occurs on the plains to reduce the energy.

The CIN on the plains is less than 40 J kg^{-1} for the whole MTP period and shows a marked decrease before MTP hour 1 (Figure 5b), suggesting favorable convective conditions along with the high CAPE in those hours. In contrast, the CIN on the mountains is above 80 J kg^{-1} and only slightly decreases in the first few hours. In a clear contrast to the MTP, the CINs in NULL for both mountains and plains are much bigger with similar magnitudes to those of WSA.

A comparison of the 0–6 km shear between the mountains and the plains (Figure 5c) shows a significant difference. The shear over the plains is significantly higher than that of the WSA for the first MTP hours, while the shear over the mountains is smaller than that of the WSA except for the first few hours. The shear over the plains remains above 15 m s^{-1} before the convection moves to the plains at MTP hour 0. The shear in both regions decreases rapidly (0 to 2 MTP hours on the plains and –3 to 0 MTP hours on the mountains) due to low-level cooling by convection. In the last three MTP hours, the magnitude of the shear on the

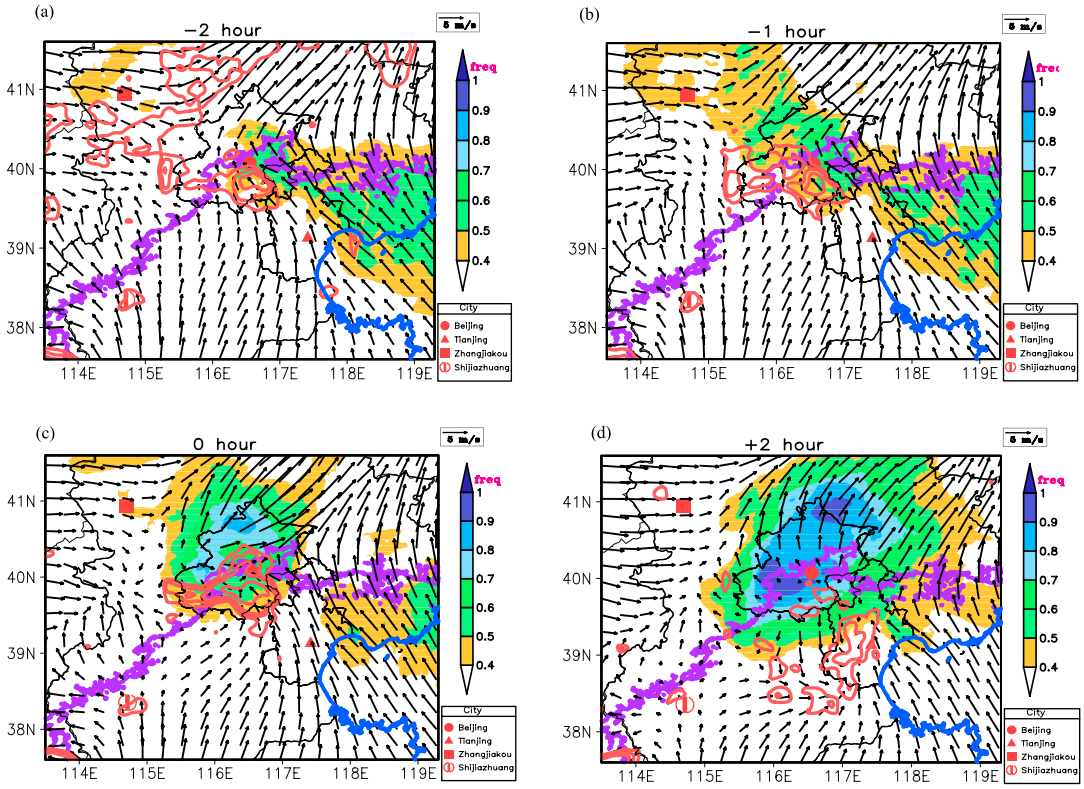

Figure 9. As in Figure 8 but for MTP case days at MTP hours (a) −2, (b) −1, (c) 0, and (d) +2. The blue line indicates the coastline of the Bohai Sea. Convergence exceeding $0.4 \times 10^{-3}\,s^{-1}$ is shown by red contours when its occurrence frequency exceeds 40% (contour interval is 10%).

plains is very close to the WSA, indicating that shear does not play an important role in the propagation of storms at this later stage. It is interesting to see that in NULL the magnitude of the shear on the plains is much lower than that in MTP (11 ms^{-1} versus 17 $m\,s^{-1}$ in the earlier hours). While the shear on the plains in the MTP cases is noticeably higher than that on the mountains, the opposite is shown in the null cases.

By examining the low-level winds, we also found large differences between the MTP and NULL/WSA, as shown in Figure 6. The wind speeds (Figure 6a) over the mountains and the plains on the MTP days are both significantly larger than their WSA and NULL counterparts. In the initial hours the difference in wind speed between the MTP days and the WSA is larger on the plains than on the mountains, indicating larger than average environmental wind speed over the plains on the MTP days. The wind direction (Figure 6b) shows that the environmental wind over the plains is largely southerly, whereas over the mountains it is mainly southwesterly. Since there is no clear WSA-prevailing wind direction, the wind direction of WSA is not shown in Figure 6b. For the null cases, the direction is quite similar to that of MTP in the first few hours. However, as shown in Figure 6a, the strength of the wind speed is much weaker than that of MTP.

The above analysis suggests that the high shear and CAPE along with low CIN over the plains characterize the MTP storm environment. The air over the plains is much more unstable with a maximum mean CAPE about 1000 $J\,kg^{-1}$ higher than over the mountain area. On the other hand, the CIN over the plains is between 2 and 4 times lower than over the mountains. The maximum shear difference is about 7 $m\,s^{-1}$. Wind speeds are greater than average over both the mountain and plain regions. The low-level wind over the plains is southerly. Although the null cases show similar a magnitude of CAPE on the mountains in the early MTP hours, the CIN (especially higher on the plains of NULL than MTP), shear (especially on the plains), and low-level wind speed are much different. These differences provided evidences of the unique characteristics of the MTP storms. The most significant difference is in the CIN over the plains between MTP and NULL, which no doubt plays an important role in determining if storms will survive and make the passage from the mountains to plains.

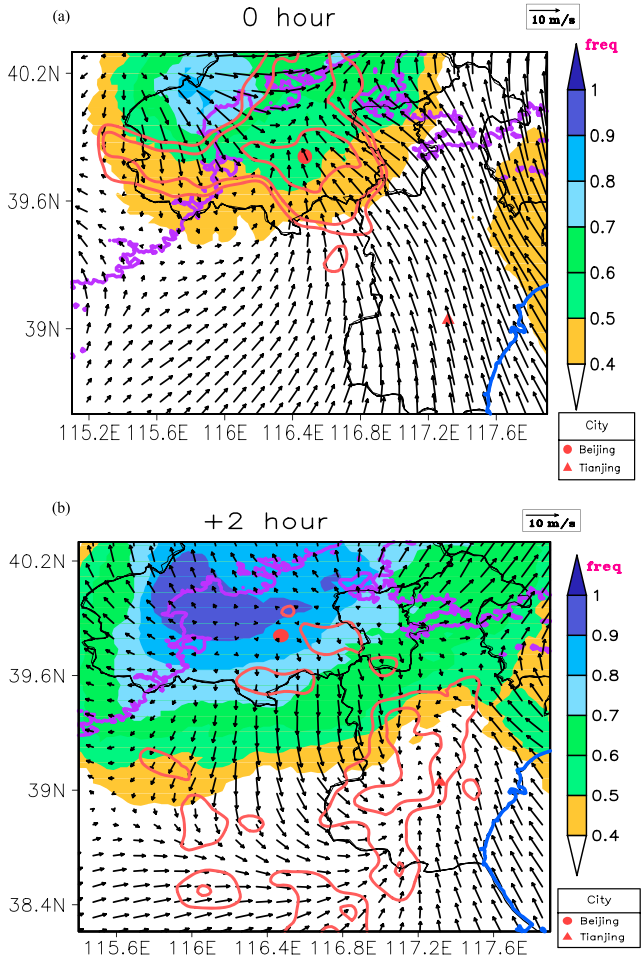

Figure 10. (a) As in Figure 9b but for a different subdomain zooming at Beijing and Tianjin; (b) as in Figure 9c but for the same subdomain in Figure 10a.

6. Mesoscale Dynamical Processes

In the previous section, we diagnosed the mean dynamic and thermal properties for the mountain and plain regions separately to examine the characteristics of the favorable large-scale environment for MTP storms. In this section we investigate major mesoscale processes that play a role in producing the precipitation pattern displayed in Figure 3. We do so by examining the spatial distribution of the low-level (250 m, the lowest VDRAS analysis level) wind, temperature, water vapor, and relative humidity fields averaged over the MTP cases. Our focus here is on the east-southeastward convective development path. We speculate that the eastward path is strongly influenced by small-scale variations of the terrain in the narrow valley between the northwest and northeast mountain ranges. The current resolution of observations and analysis is not capable of resolving the dynamic processes associated with the convective development in that region.

The mean perturbation temperature at low level, along with the wind vectors, is shown in Figures 7a, 7b, and 7c for three different times of the MTP cases, and Figures 7d and 7e for two different times of the null cases. The mean perturbation temperature was computed as follows. First, the perturbation temperature was obtained by subtracting the horizontal mean temperature from each VDRAS temperature analysis; second, the perturbation temperature at different MTP times is averaged over all selected cases. Before the convection moves to the plains (Figure 7a), the plains are dominated by southerly and southeasterly winds. The MTP wind on the plains is much stronger than the WSA shown in Figure 8. The strong southeasterly wind over the Bohai Sea may at least partly be the effect of the sea breeze, which encroaches on the land as clearly seen in the WSA (Figure 8). At −2 MTP hours (Figure 7a) there is a cold air mass near the ZBRC radar location in Zhangjiakou, resulting likely from evaporation of the scattered convective activity on the mountains. Another cold air mass is clearly shown over the foothills in Beijing, caused by cloudiness and precipitation associated with upslope lifting. The two cold air masses merge into one in the next 2 h, forming a strengthened cold pool (Figure 7b) corresponding to the enhanced convective activity shown in Figure 4b. The northwesterly outflows on the southwest flank of the cold pool increase the convergence on the slope near the 200 m contour. The cold pool strengthens further and advances toward the plains in the next 2 MTP hours (Figure 7c), pushing the convergence zone to Tianjin and Hebei, and resulting in significant changes in wind direction over a large area of the plains due to the storm outflows.

A striking difference between the MTP and NULL cases is the lack of the cold pool in NULL (compare Figures 7a and 7d, and Figures 7b with 7e, respectively). Another clear difference is the weaker winds in NULL. The wind over the Bohai Sea encroaches only the coastline, similar as in the WSA (Figure 8), indicating the relative weak sea breeze. At −2 MTP hours (Figure 7d) there is only a very weak cold air mass and weak northwest winds near the ZBRC radar location in Zhangjiakou. The magnitude of the cold air mass

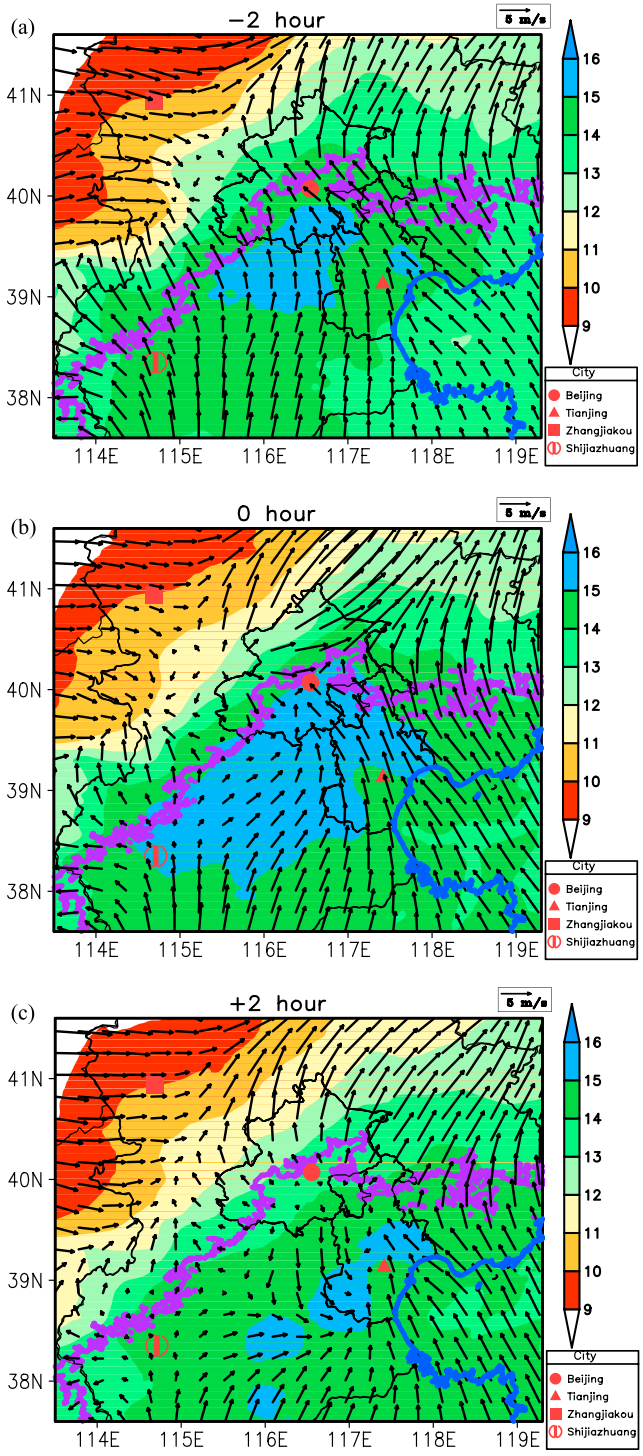

Figure 11. As in Figure 9 but for hourly averaged water vapor mixing ratio (g kg^{-1}) on 250 m above the surface at MTP hours (a) −2, (b) 0, and (c) +2.

increases at 0 MTP hour when moved to the north of Beijing (Figure 7e) but is not strong enough to form a significant cool pool as for the MTP cases. As a result, there is no strong westerly wind to increase the convergence on the slope as in MTP, resulting in less frequency of storms compared to MTP. Consequently, the convection is unable to strengthen and reach the plains.

To further illustrate the role of the cold pool on the strengthening of the MTP storms as they move down the slope and to the plains, the frequency of occurrence of a cold air anomaly with temperature below −3°C is computed and shown in Figure 9 along with the convergence (negative divergence) frequency associated with the cold pool front. At −2 MTP hours, large convergence appears over the mountains and on the slopes in southern Beijing where the strong upslope southeasterly wind prevails (Figure 9a). At −1 and 0 MTP hours, the convergence over the mountains weakens while that over southern Beijing expands (Figures 9c and 10a for a close-up view). Meanwhile, the region of frequent occurrence of the −3°C cold pool also enlarges during this time. The area of high convergence then propagates to central Tianjin in the next MTP hour (Figures 9d and 10b for a close-up view). The regions of high convergence over southern Beijing and over central Tianjin (Figures 9c and 9d) correspond quite well to the two high-frequency centers of 40 dBZ convection on the east-southeastward shown in Figures 3 and 4c.

Figure 11a shows an area with mean water vapor mixing ratio larger than 15 g kg^{-1} south of Beijing at −2 MTP hours, corresponding to high relative humidity in Figure 12a. This could be a result of moisture convergence due to blocking of the south-southeasterly winds by the mountains and the cool air mass on the foothills. The areas of high water vapor mixing ratio and relative humidity both significantly expand at 0 MTP hours (Figures 11b and 12b) to cover both southern Beijing and a large part of Tianjin, favoring convective initiation in these two regions. In the next 2 h, the vapor mixing ratio in the storm outflow region decreases, although it is nearly saturated (Figure 11c) due to the drop in temperature corresponding to the cold pool.

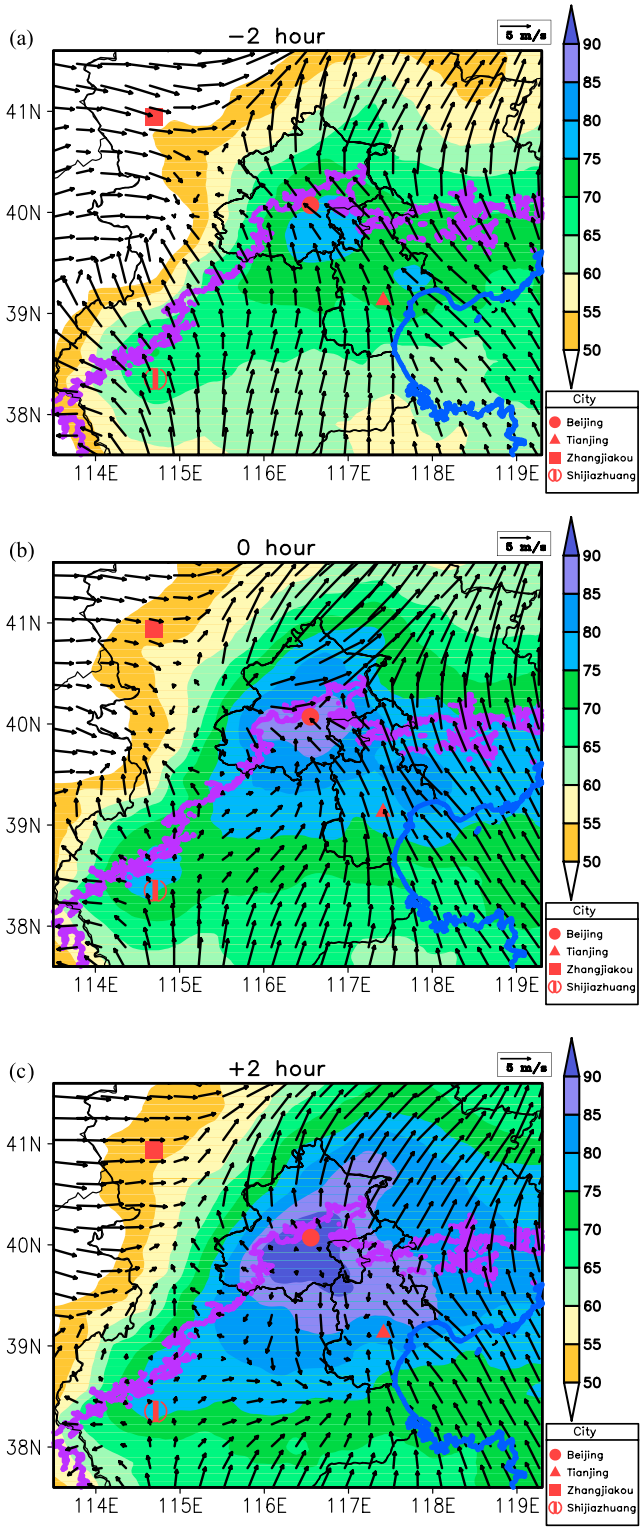

Figure 12. As in Figure 11 but for the average relative humidity (%).

To reveal the vertical distribution of the cold pool and the vertical motion, two cross sections of the mean perturbation temperature, vertical velocity, and wind vectors along the line A–B in Figure 7a and the line C–D in Figure 7b are shown in Figures 13 and 14, respectively. From the −2 to 0 MTP hours (Figures 13a and 13b), the A–B cross section shows the merging and strengthening of the two cold air masses originated from the mountains and the foothills, respectively, as well as the downward motion on the left flank (northwest) of the cold pool and upward motion on the right flank (southeast) of the cold pool (Figure 13b). Similarly, Figure 14 shows that from the 0 to +2 MTP hours (Figures 14a and 14b) the cold pool in Figure 13b is advanced southeastward resulting in strengthened lifting at the location of the sea breeze front.

The above examination of the mean spatial distribution of the wind, temperature, and humidity suggests that the formation of the cold pool and the enhancement of convergence by its outflows not only play a critical role in convective initiation on the slopes but also in subsequent strengthening of the convection over the plains. The preferred location of convection near the southern border of Beijing is associated with the enhanced convergence between the storm outflow and southerly wind in Hebei province, while the high frequency of convection near central Tianjin corresponds well with convergence between the storm outflow and southeasterly flow from the Bohai Sea.

7. Summary and Conclusions

Eighteen cases of MTP-propagating storms in the absence of strong synoptic forcing were chosen to study the features of these storms using rapid-update VDRAS reanalyses. We first computed the frequency of occurrence of 40 dBZ reflectivity for the 18 cases to show the propagation and initiation characteristics of these convective systems and found that the MTP convective storms occur along two major paths: east-southeastward and eastward. The east-southeastward path corresponds to storms propagating and strengthening on the plains from south Beijing to Tianjin, while the eastward path occurs over the complex terrain between two

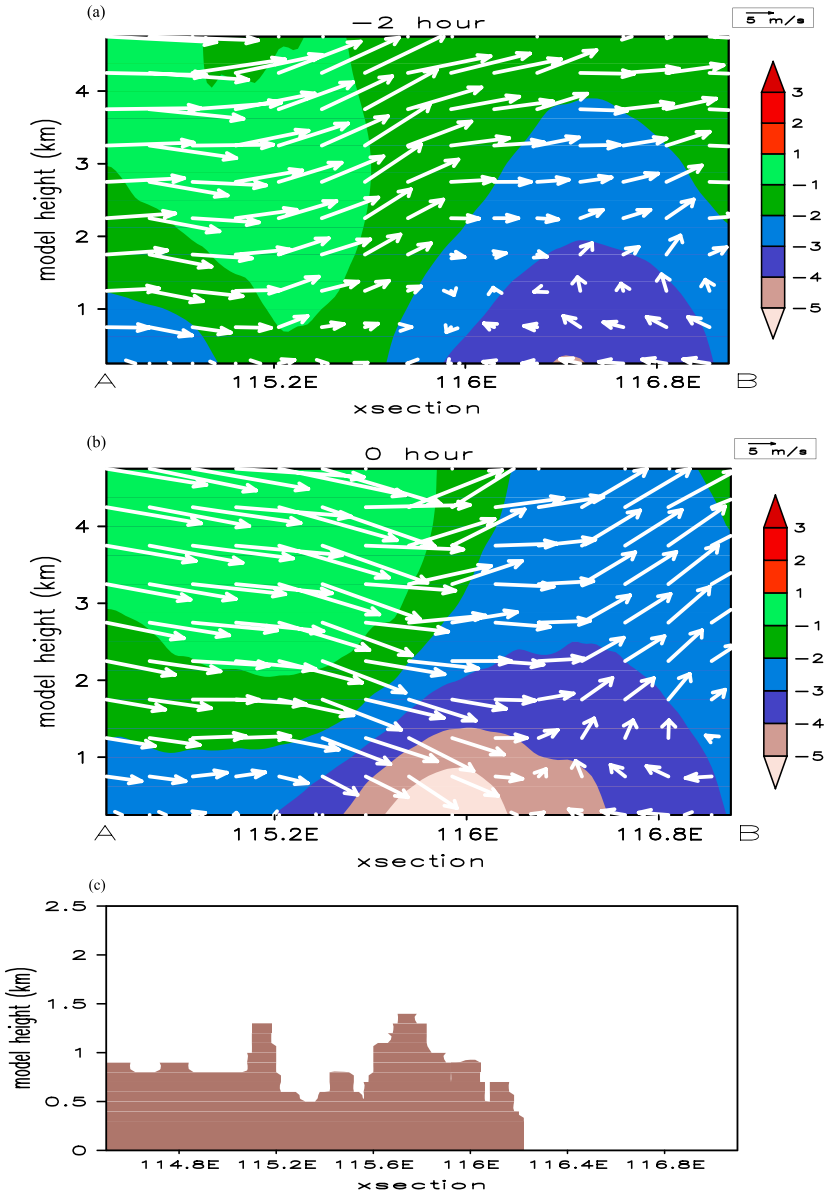

Figure 13. Average perturbation temperature (color shading; °C) shown in the cross section along A–B in Figure 7a, overlain with mean wind (vectors) and vertical speed (contour, orange is positive and red is negative) for the MTP hours (a) −2 and (b) 0. (c) The corresponding terrain.

mountain ranges to the northeast and east of Beijing. We then examined the mean characteristics of CAPE, CIN, vertical shear, and low-level wind on the mountains and the plains using the warm season (15 June to 15 September 2013) as a baseline. To further illustrate the distinct characteristics of the MTP storms, we contrasted these mean characteristics with those from a set of null cases in which the mountain-initiated storms dissipated before reaching the plains. Finally, we showed the spatial distribution of the low-level wind, temperature, and humidity averaged over the 18 days of VDRAS reanalyses in an attempt to investigate the dynamical mechanisms of the east-southeastward path.

The spatial analysis of storm frequencies suggests that most storms are found to the southeast and northeast of Beijing after reaching the plains. The temporal evolution of hourly storm frequencies indicates that the subsequent evolution of the MTP convective systems has three stages: initiation over the mountains near the Zhangbei radar station, intensification along the foothills, and division into two paths and three high-frequency centers, located east and southeast of Beijing and around the center of Tianjin.

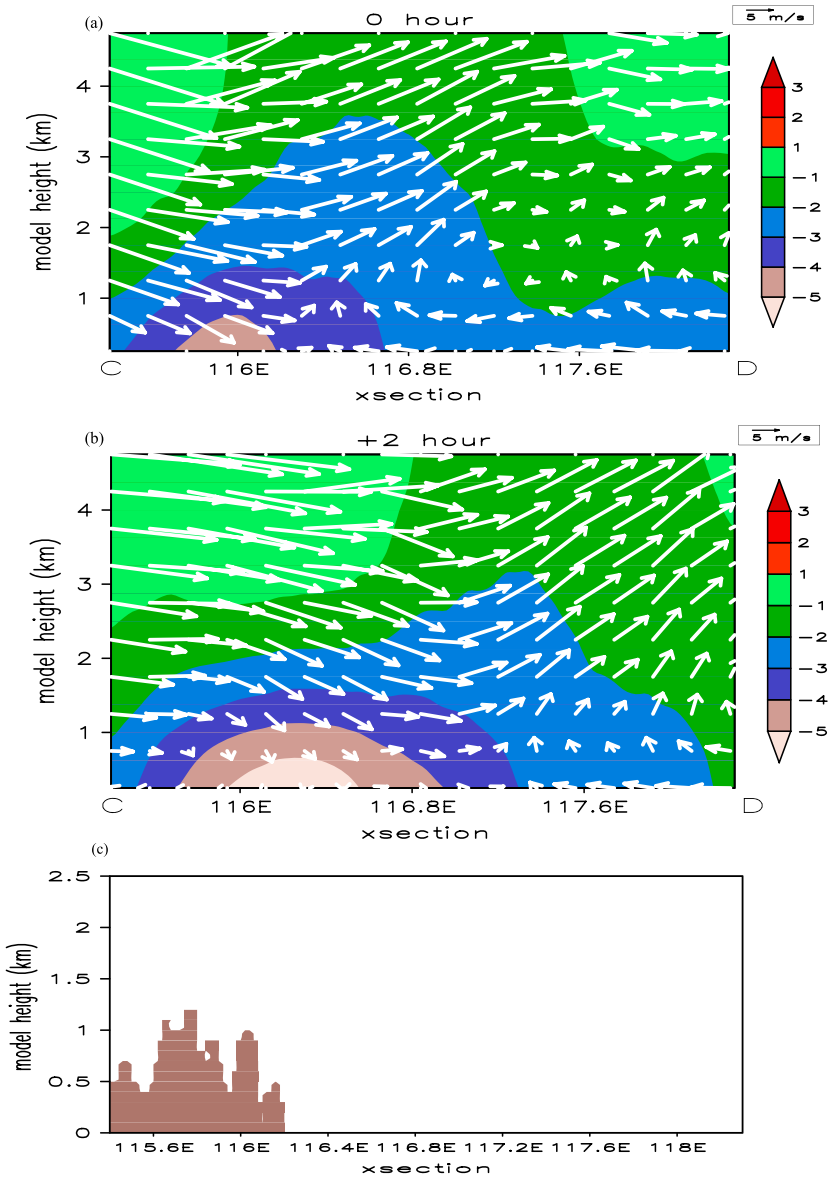

Figure 14. The same as Figure 13 but for cross section along C–D in Figure 7b for the MTP hour (a) 0 and (b) +2.

Distinct features were found by comparing the mountain and plain CAPE, CIN, vertical shear, and low-level wind. Over the plains the CAPE is significantly higher than over the mountains, and the CIN is much lower. Both the CAPE and CIN over the two regions are very different from the warm season averages. The vertical shear over the plains is significantly higher than over the mountains and the warm season average. The prevailing environmental winds over the mountains and over the plains are much stronger than the warm season average. The wind direction over the mountains is predominantly southwesterly and over the plains is southerly. The comparison of the mean CAPE, CIN, and low-level wind of the MTP storms with those from the null cases showed that, although the null cases have similar magnitude of CAPE to that of the MTP cases on the mountains, they display quite different characteristics in terms of the CIN, low-level wind speed, and shear from those of the MTP cases. We believe the above findings provide very useful guidance for improving the intensification/decay forecast of the weakly forced, mountain-initiated storms.

The mean spatial distributions of wind, temperature, and humidity revealed that the MTP storms are associated with strong cold pools, their resulting outflows, and high humidity. The cold pools are originally produced over the mountains from evaporative cooling of convection, then propagate downslope to

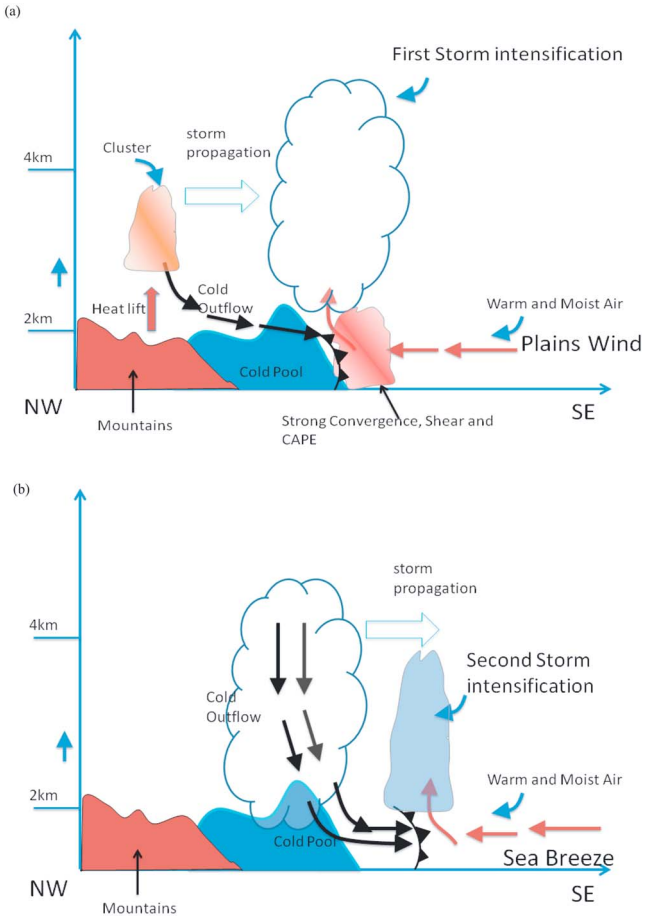

Figure 15. Schematic illustration of the interaction of outflows, cool air, and environmental wind in the intensification of MTP convection. (a) The first intensification of MTP storms from mountains to plains south of Beijing, and (b) the second intensification near Tianjin.

merge with the cold air mass on the foothills, and finally strengthen over the plains. The strong cold pool outflows near the surface generate significant convergence with the southerly and southeasterly environmental flows at the edge of the cold pool, creating updraft under unstable conditions (high CAPE and shear). The enhanced convergence between the northwesterly storm outflow and the southerly environmental wind south of Beijing corresponds well with the high frequency of convection near the southern border of Beijing (the first storm intensification in Figure 15a). By comparing the mean wind of the MTP days with that of the warm season average and the null cases, we found that the sea breeze from the Gulf of Bohai Sea may play a role in the strong southeasterly wind that is essential for creating the convergence in Tianjin as the MTP storms arrive at the plains, resulting in the high frequency of convection near Tianjin (the second storm intensification in Figure 15b).

We have not studied the dynamical features of the eastward path storms that occur over the mountainous region north and northeast of Beijing because of the lack of radar observations in that region and the complex and fine-scale terrain variations at the intersection of two mountain ranges. The BMS is in the process of installing X band Doppler radars near the valley between the two mountain ranges. Our plan is to assimilate the observations from the X band radar when they become available along with the existing radar network to create a higher-resolution VDRAS reanalysis to study the dynamical features and formation mechanism of the storms taking the eastward path. Another topic that deserves a detailed study in our future work is the role of the urban effects in the convective process. *Yang et al*. [2014a] suggested that the combination of a sea breeze and urban effects could result in convective intensification. Higher-resolution model runs with and without the urban land use are being conducted for a convective case with clear urban influences.

The role of cold pools in convective initiation has been studied previously using model simulations [i.e., *Rotunno et al*., 1988; *Fovell and Tan*, 1998; *Lin et al*., 1998; *Jeong et al*., 2016]. Our current study is unique because the statistical analysis of the multiple cases is based on the VDRAS reanalyses that combine a cloud model with radar observations using the advanced 4DVAR technique. The consistency of the results with radar reflectivity confirms the important role of cold pools in convective initiation.

Acknowledgments
This work was funded by the China Special Fund for Meteorological Research in the Public Interest (GYHY201306008, GYHY201506004, and GYHY200906026), the National Natural Science Foundation of China (41305041 and 41575050), the National Basic Research Program of China ("973", 2014CB441406), and the Beijing Natural Science Foundation (8162018). The authors would like to thank Jim Wilson and two anonymous reviewers for providing thorough reviews that greatly helped us improve the manuscript. The data for this paper are available at Urban Meteorological Data Center of IUM (http://www.ium.cn/en).

References

Carbone, R. E., and J. D. Tuttle (2008), Rainfall occurrence in the U.S. warm season: The diurnal cycle, *J. Clim.*, *21*(16), 4132–4146, doi:10.1175/2008JCLI2275.1.

Carbone, R. E., J. D. Tuttle, D. A. Ahijevych, and S. B. Trier (2002), Inferences of predictability associated with warm season precipitation episodes, *J. Atmos. Sci.*, *59*(13), 2033–2056, doi:10.1175/1520-0469(2002)059<2033:IOPAWW>2.0.CO;2.

Chen, M., Y.-C. Wang, F. Gao, and X. Xiao (2012), Diurnal variations in convective storm activity over contiguous north China during the warm season based on radar mosaic climatology, *J. Geophys. Res.*, *117*, D20115, doi:10.1029/2012JD018158.

Chen, M., Y. Wang, F. Gao, and X. Xiao (2014), Diurnal evolution and distribution of warm-season convective storms in different prevailing wind regimes over contiguous north China, *J. Geophys. Res. Atmos.*, *119*, 2742–2763, doi:10.1002/2013JD021145.

Chen, M., X. Xiao, F. Gao, and Y. Wang (2016), A case study and batch verification on high resolution numerical simulations of severe convective events using an analysis system based on rapid-refresh 4-D variational radar data assimilation [in Chinese with English abstract], *Acta Meteorol. Sin.*, *74*(3), 421–441.

Chen, X., K. Zhao, J. Sun, B. Zhou, and W. -C. Lee (2016), Assimilating surface observations in a four-dimensional variational Doppler radar data assimilation system to improve the analysis and forecast of a squall line case, *Adv. Atmos. Sci.*, *33*(10), 1106–1119.

Crook, N. A., and J. Sun (2002), Assimilation radar, surface and profiler data for the Sydney 2000 forecast demonstration project, *J. Atmos. Oceanic Technol.*, *19*, 888–898, doi:10.1175/1520-0426(2002)019<0888:ARSAPD>2.0.CO;2.

Davis, C. A., K. W. Manning, R. E. Carbone, S. B. Trier, and J. D. Tuttle (2003), Coherence of warm-season continental precipitation in numerical weather prediction models, *Mon. Weather Rev.*, *131*(11), 2667–2679, doi:10.1175/1520-0493(2003)131<2667:COWCRI>2.0.CO;2.

Dixon, M., and G. Wiener (1993), TITAN: Thunderstorm identification, tracking, analysis, and nowcasting—A radar-based methodology, *J. Atmos. Oceanic Technol.*, *10*(6), 785–797, doi:10.1175/1520-0426(1993)010<0785:TTITAA>2.0.CO;2.

Dou, J., Y. Wang, R. Bornstein, and S. Miao (2014), Observed spatial characteristics of Beijing urban climate impacts on summer thunderstorms, *J. Appl. Meteorol. Climatol.*, *54*(1), doi:10.1175/JAMC-D-13-0355.1.

Fovell, R. G., and P.-H. Tan (1998), The temporal behavior of numerically simulated multicell-type storms. Part II: The convective cell life cycle and cell regeneration, *Mon. Weather Rev.*, *126*(11), 551–577, doi:10.1175/15200469(1995)052<2073:TTBONS>2.0.CO;2.

Friedrich, K., E. A. Kalina, J. Aikins, D. Gochis, and R. Rasmussen (2015), Precipitation and cloud structures of intense rain during the 2013 Great Colorado Flood, *J. Hydrometeorol.*, *17*(1), 22–27, doi:10.1175/JHM-D-14-0157.1.

Gochis, D., et al. (2015), The Great Colorado Flood of September 2013, *Bull. Am. Meteorol. Soc.*, *96*(9), 1461–1487, doi:10.1175/BAMS-D-13-00241.1.

He, H., and F. Zhang (2010), Diurnal variations of warm-season precipitation over northern China, *Mon. Weather Rev.*, *138*(4), 1017–1025, doi:10.1175/2010MWR3356.1.

He, J., Z. Wu, Z. Jiang, C. S. Miao, and G. R. Han (2007), "Climate effect" of the northeast cold vortex and its influences on Meiyu, *Chin. Sci. Bull.*, *52*(5), 671–679.

Hu, H. (2015), Spatiotemporal characteristics of rainstorm-induced hazards modified by urbanization in Beijing, *J. Appl. Meteorol.*, *54*(7), 1496–1509.

Huang, R. (2012), Features of intensifying thunderstorms moving down from the mountains and case study in Beijing, M.Sc. thesis [in Chinese], Chin. Acad. of Meteorol. Sci., Beijing.

Jeong, J., D. Lee, and C. Wang (2016), Impact of cold pool on mesoscale convective system produced extreme rainfall over southeastern South Korea: 7 July 2009, *Mon. Weather Rev.*, doi:10.1175/MWR-D-16-0131.1, in press.

Ji, X., W. Hu, S. Ma, X. Pei, J. Mu, and J. Ma (2008), Comparative analysis of two typical hail weather in Ningxia under influence of cold vortex over Mongolia, *J. Nat. Disasters*, *17*(2), 103–109.

Koo, M.-S., and S.-Y. Hong (2010), Diurnal variations of simulated precipitation over East Asia in two regional climate models, *J. Geophys. Res.*, *115*, D05105, doi:10.1029/2009JD012574.

Lin, P.-F., P.-L. Chang, B. J.-D. Jou, J. W. Wilson, and R. D. Roberts (2011), Warm season afternoon thunderstorm characteristics under weak synoptic-scale forcing over Taiwan island, *Weather Forecasting*, *26*(1), 44–60, doi:10.1175/2010WAF2222386.1.

Lin, Y.-L., R. L. Deal, and M. S. Kulie (1998), Mechanisms of cell regeneration, development, and propagation with a two-dimensional multicell storm, *J. Atmos. Sci.*, *55*(10), 1867–1886, doi:10.1175/1520-0469(1998)055<1867:MOCRDA>2.0.CO;2.

Liu, D., X. Qie, Y. Xiong, and G. Feng (2011), Evolution of the total lightning activity in a leading-line and trailing stratiform mesoscale convective system over Beijing, *Adv. Atmos. Sci.*, *28*(4), 866–878.

Liu, D., X. Qie, L. Pan, and L. Peng (2013), Some characteristics of lightning activity and radiation source distribution in a squall line over north China, *Atmos. Res.*, *132–133*, 423–433.

Mather, G. K., D. Treddenick, and R. Parsons (1976), An observed relationship between the height of the 45 dBZ contours in storm profiles and surface hail reports, *J. Appl. Meteorol.*, *15*(12), 1336–1336.

Miao, S.-G., F. Chen, Q.-C. Li, and S. Fan (2011), Impacts of urban processes and urbanization on summer precipitation: A case study of heavy rainfall in Beijing on 1 August 2006, *J. Appl. Meteorol. Climatol.*, *50*(4), 806–825, doi:10.1175/2010JAMC2513.1.

Murphy, M. S., and C. E. Konrad II (2005), Spatial and temporal patterns of thunderstorm events that produce cloud-to-ground lightning in the interior southeastern United States, *Mon. Weather Rev.*, *133*(6), 1417–1430, doi:10.1175/MWR2924.1.

Overeem, A., I. Holleman, and A. Buishand (2009), Derivation of a 10-year radar-based climatology of rainfall, *J. Appl. Meteorol. Climatol.*, *48*(7), 1448–1463, doi:10.1175/2009JAMC1954.1.

Parker, M. D., and J. C. Knievel (2005), Do meteorologists suppress thunderstorms?: Radar-derived statistics and the behavior of moist convection, *Bull. Am. Meteorol. Soc.*, *86*(3), 341–358, doi:10.1175/BAMS-86-3-341.

Rickenbach, T., and S. Rutledge (1998), Convection in TOGA COARE, horizontal scale, morphology, and rainfall production, *J. Atmos. Sci.*, *55*(17), 2715–2729, doi:10.1175/1520-0469(1998)055<2715:CITCHS>2.0.CO;2.

Rotunno, R., J. B. Klemp, and M. L. Weisman (1988), A theory for strong, long-lived squall line, *J. Atmos. Sci.*, *45*(3), 463–485, doi:10.1175/1520-0469(1988)045<0463:ATFSLL>2.0.CO;2.

Steiner, M., R. A. Houze Jr., and S. E. Yuter (1995), Climatological characterization of three-dimensional storm structure from operational radar and rain gauge data, *J. Appl. Meteorol.*, *34*(9), 1978–2007, doi:10.1175/1520-0450(1995)034<1978:CCOTDS>2.0.CO;2.

Sun, J. (2005), Convective-scale assimilation of radar data: Progress and challenges, *Q. J. R. Meteorol. Soc.*, *131*(613), 3439–3463, doi:10.1256/qj.05.149.

Sun, J., and N. A. Crook (1997), Dynamical and microphysical retrieval from Doppler radar observations using a cloud model and its adjoint: I. Model development and simulated data experiments, *J. Atmos. Sci.*, *54*(12), 1642–1661, doi:10.1175/1520-0469(1997)054<1642:DAMRFD>2.0.CO;2.

Sun, J., and N. A. Crook (1998), Dynamical and microphysical retrieval from Doppler radar observations using a cloud model and its adjoint: II. Retrieval experiments of an observed Florida convective storm, *J. Atmos. Sci.*, *55*(5), 835–852, doi:10.1175/1520-0469(1998)055<0835:DAMRFD>2.0.CO;2.

Sun, J., and N. A. Crook (2001), Real-time low-level wind and temperature analysis using single WSR-88D data, *Weather Forecasting*, *16*(1), 117–132.

Sun, J., and Y. Zhang (2008), Analysis and prediction of a squall line observed during IHOP using multiple WSR-88D observations, *Mon. Weather Rev.*, *136*(7), 2364–2388, doi:10.1175/2007MWR2205.1.

Sun, J., M. Chen, and Y.-C. Wang (2010), A frequent-updating analysis system based on radar, surface, and mesoscale model data for the Beijing 2008 Forecast Demonstration Project, *Weather Forecasting*, *25*(6), 1715–1735, doi:10.1175/2010WAF2222336.1.

Surcel, M., M. Berenguer, and I. Zawadzki (2010), The diurnal cycle of precipitation from continental radar mosaics and numerical weather prediction models. Part I: Methodology and seasonal comparison, *Mon. Weather Rev.*, *138*(8), 3084–3106, doi:10.1175/2010MWR3125.1.

Tai, S.-J., Y.-C. Liou, J. Sun, S.-F. Chang, and M.-C. Kuo (2011), Precipitation forecasting using Doppler radar data, a cloud model with adjoint, and the Weather Research and Forecasting model: Real case studies during SoWMEX in Taiwan, *Weather Forecasting*, *26*(6), 975–992, doi:10.1175/WAF-D-11-00019.1.

Wang, C.-C., G. T.-J. Chen, and R. E. Carbone (2004), A climatology of warm-season cloud patterns over East Asia based on GMS infrared brightness temperature observations, *Mon. Weather Rev.*, *132*(7), 1606–1629, doi:10.1175/1520-0493(2004)1322.0.CO;2.

Wilson, J. W., Y. Feng, M. Chen, and R. D. Roberts (2010), Nowcasting challenges during the Beijing Olympics: Successes, failures, and implications for future nowcasting systems, *Weather Forecasting*, *25*(6), 1691–1714, doi:10.1175/2010WAF2222417.1.

Yang, L., J. A. Smith, L. Yang, J. A. Smith, M. L. Baeck, E. Bou-Zeid, S. M. Jessup, F. Tian, and H. Hu (2014a), Impact of urbanization on heavy convective precipitation under strong large-scale forcing: A case study over the Milwaukee-Lake Michigan Region, *J. Hydrometeorol.*, *15*, 261–278, doi:10.1175/JHM-D-13-020.1.

Yang, L., F. Tian, J. A. Smith, and H. Hu (2014b), Urban signatures in the spatial clustering of summer heavy rainfall events over the Beijing metropolitan region, *J. Geophys. Res. Atmos.*, *119*, 1203–1217, doi:10.1002/2013JD020762.